The Journal of Green Energy and Environmental Engineering

Research Paper

$CDsCuO_x$ Nanocomposites for Peroxydisulfate Activation Toward Tetracycline Degradation

Karin Rodríguez[1], Mina Andolar[1], Poul Hakkarainen[1,*]

[1] Department of Chemistry, Chaudhary Charan Singh Haryana Agricultural University, Hisar, Haryana 125001, India
*Corresponding author: Karinrodríguez@gmail.com; MAndolar@hau.ac.in; PHakkarainen@hau.ac.in

Abstract. The construction of abundant active sites and enhancement of pollutant-specific selectivity on heterogeneous catalyst surfaces are crucial for efficient pollutant removal via persulfate-based advanced oxidation processes. The incorporation of carbon dots (CDs) into copper-based oxides to construct multivalent metal species can significantly improve the activation capability of peroxydisulfate (PS). In this study, a simple calcination method is employed to regulate the valence state of Cu in copper-based oxides using CDs, resulting in the synthesis of a CDs/CuO composite with multiphase structures comprising Cu^0, Cu_2O, and CuO. In the degradation of tetracycline (TC) (used as a model pollutant), the CDs/CuO composite exhibits excellent activation capability. Under the reaction conditions of TC concentration (50 mg/L), PS concentration (0.5 mmol/L), and catalyst concentration (0.06 g/L), the degradation efficiency of TC reaches 99% within 60 min, with an apparent reaction rate constant of 0.066 min^{-1}. This reaction rate is 6.6 times that of pure CuO. Cu^0 acts as a continuous electron donor, not only inducing the generation of selective singlet oxygen ($^1O_2$) but, more importantly, promoting the Cu^{2+}/Cu^+ cycle reaction. This cycle generates hydroxyl radicals (·OH) and improves activation efficiency. The use of CDs regulates the coexistence of multivalent Cu active sites in the catalyst, which enhances the activation capability for PS, providing a new idea for the efficient design of catalysts.

Keywords: *carbon dots; copper based compound; activation; peroxydisulfate; tetracycline*

Received on 02 March 2023, Accepted on 28 May 2023, Published on 15 July 2023

1 Introduction

Tetracycline hydrochloride (TC), as a key member of broad-spectrum antibiotics, is widely used in medical, livestock, and agricultural fields due to its low cost, high activity, and excellent anti-inflammatory effects[1]. However, discharged antibiotics are difficult to degrade and accumulate through the food chain, posing significant threats to public health and ecological security. Current methods for degrading antibiotics in wastewater mainly include physical methods[2] and chemical methods[3]. Traditional physical methods suffer from poor recyclability of adsorbents and non-biodegradability of organic pollutants. Traditional chemical methods, primarily Fenton reactions, generate hydroxyl radicals (·OH) to oxidatively degrade pollutants. These methods are limited by high consumption of H_2O_2 and metal ions, a narrow effective pH range, and the generation of large amounts of sludge after reaction. Therefore, there is an urgent need to explore an efficient and economical strategy for degrading antibiotics in wastewater. In recent years, persulfate-based advanced oxidation processes have emerged as an effective degradation strategy[4-5]. The reactive oxygen species generated in this process possess high reactivity and oxidizing capacity, enabling non-selective attack on most organic pollutants to achieve degradation. Activation of persulfate can be achieved through external energy sources such as ultraviolet light[6], heat[7], and ultrasound[8], or via catalysts to break the peroxide bonds in PS, thereby generating highly active radicals. Among these radicals, the sulfate radical ($SO_4\cdot^-$) has a higher redox potential (E^o = 2.5–3.1 V) than the hydroxyl radical (·OH) (E^o = 1.89–2.72 V), along with a longer half-life (30–40

μs)[9]. Methods using thermal or UV activation are often cumbersome to operate and entail high maintenance costs; thus, catalyst activation is a feasible and effective approach.

Among heterogeneous catalysts, transition metal-based catalysts have garnered widespread attention due to their high catalytic activity. Metals extensively studied include Fe, Co, Mn, and Cu. The sole use of the first three metals often encounters issues such as low reaction activity and high metal leaching during activation[10-11]; hence, composite multi-metal materials are often employed to improve degradation efficiency. In recent research, a Co-N@MoS_2-COOH catalyst containing both sulfur vacancies (V_S) and nitrogen vacancies (V_N) was fabricated. V_S and V_N induced the generation of superoxide radicals ($O_2\cdot^-$) and $^1O_2$, while the bimetallic electron pump promoted persulfate decomposition; these synergistic effects achieved pollutant degradation[12]. Compositing high-entropy perovskite oxides (HEPs) with carbon microspheres (CS) formed an HEPs@CS catalyst. The multi-metallic composition of HEPs created electron transfer pathways, promoted dynamic cycling of metal valences, maintained continuous catalytic reactions, and effectively degraded Rhodamine B (RhB)[13]. Research on Cu-activated persulfate dates back several decades. Elemental Cu^0 exhibits low activation capability, and the Cu^+ structure is unstable; thus, studies using Cu^{2+} to activate persulfate are most prevalent[14-15]. CuO possesses strong electron transfer capability and can activate PS through multiple pathways. For instance, Huang et al.[16] proposed that the Cu^{2+} structure in CuO can abstract electrons from electron-rich organic substrates like phenol, forming reactive phenoxy radical intermediates, thereby effectively activating PS to selectively degrade phenolic/aniline compounds in wastewater. Xu et al.[17] suggested that negatively charged PS can adsorb onto the positively charged CuO surface to form an activated PS state for pollutant degradation. To mitigate Cu ion leaching, Zhang et al.[18] loaded CuO onto magnesium-aluminum layered double hydroxide (LDH) with high alkalinity to prepare a Cu/LDH catalyst. This catalyst featured a larger specific surface area, higher alkalinity, and more exposed active sites, enabling efficient PS activation for ciprofloxacin degradation. There are also reports on biochar-supported bimetallic Fe_3O_4-CuO (CuFeBC) catalysts for PS activation to degrade norfloxacin[19]. The functional groups on biochar not only accelerated electron transfer but also effectively reduced metal leaching from the catalyst, maintaining good catalytic activity.

Carbon dots (CDs) are novel zero-dimensional carbon-based nanomaterials characterized by high-density active sites, excellent electron transfer capability, and good functionalization potential, which are advantageous for catalysis[20]. Therefore, theoretically, utilizing CDs to modulate CuO is feasible for obtaining catalysts with high activation capability. In this study, the reductive properties of CDs were leveraged to regulate the valence state of Cu in copper-based oxides, yielding a nanocomposite CDs/CuO_x composed of Cu^0, Cu_2O, and CuO. In the PS activation system for TC degradation, Cu^0 serves as a continuous electron donor. The generated $O_2\cdot^-$ not only produces selective $^1O_2$ but, more crucially, promotes the Cu^{2+}/Cu^+ cycle reaction, thereby enhancing activation efficiency. This strategy of utilizing CDs to regulate Cu valence states in catalysts to achieve coexistence of multiple activation pathways provides new insights for efficient PS activation.

2 Experimental Materials and Methods

2.1 Raw Materials

Anhydrous citric acid, ethylenediamine, urea, $Cu(NO_3)_2\cdot 3H_2O$, tetracycline hydrochloride, sodium peroxydisulfate, furfuryl alcohol (FFA), p-benzoquinone (BQ), and methanol (MeOH, chromatographic grade) were all purchased from Aladdin Biochemical Technology Co., Ltd. (Shanghai, China). tert-Butyl alcohol (TBA) and 5,5-dimethyl-1-pyrroline N-oxide (DMPO, purity ≥ 97%) were procured from Macklin Biochemical Co., Ltd. (Shanghai, China). All chemical reagents were of analytical grade or higher and were used without further purification.

2.2 Experimental Methods

2.2.1 Catalyst Preparation

Preparation of CDs:Following a previously reported method, CDs were synthesized via a hydrothermal route using citric acid and ethylenediamine[21]. Specifically, 2.1 g of anhydrous citric acid was dispersed in 20 mL of

deionized water, followed by the addition of 670 µL of ethylenediamine under stirring. The mixed solution was transferred into a 50 mL Teflon-lined autoclave and reacted at 180 °C for 8 h. After natural cooling to room temperature, the solution was dialyzed in a 3500 Da dialysis bag for 48 h. Finally, the dialyzed brown solution was dried at 60 °C to obtain CDs powder.

Preparation of CDs/CuO$_x$:2 mmol of $Cu(NO_3)_2 \cdot 3H_2O$ and 8 mmol of urea were dispersed in 30 mL of deionized water. Subsequently, 20, 30, or 40 mg of CDs was added to the above solution. The homogeneous mixture was transferred into a Teflon-lined autoclave and maintained at 120 °C for 12 h. After natural cooling to room temperature, the product was separated using a 0.22 µm polytetrafluoroethylene (PTFE) filter membrane, washed thoroughly, and dried at 60 °C for 12 h. The dried precipitate was then calcined in a tubular furnace under argon atmosphere protection at 300 °C for 4 h, with a heating rate of 5 °C/min. The furnace was allowed to cool naturally to obtain the final samples, denoted as CDs/CuO$_x$-20, CDs/CuO$_x$-30, and CDs/CuO$_x$-40, respectively.

Preparation of CuO:For comparative purposes, pure CuO was synthesized following the same procedure as CDs/CuO$_x$ but without the addition of CDs.

2.2.2 Material Characterization

The crystalline phases of the catalysts were analyzed using a D8 X-ray diffractometer (XRD). The specific surface area and pore size distribution were determined using a Micromeritics ASAP2020 Brunauer-Emmett-Teller (BET) surface area and porosity analyzer. The micro-morphology was observed using a JEM-2800 transmission electron microscope (TEM) and an S-4800 scanning electron microscope (SEM). Surface elemental composition and valence states were examined using a K-alpha X-ray photoelectron spectrometer (XPS). Fourier-transform infrared (FT-IR) spectra were acquired using a Nexus 670 spectrometer. Electron paramagnetic resonance (EPR) spectroscopy was performed using an EMXPLUS10/12 spectrometer to identify radical species. Residual pollutant concentrations were measured using an Essential LC-16 high-performance liquid chromatograph (HPLC). The electrochemical properties, including cyclic voltammetry (CV) and electrochemical impedance spectroscopy (EIS), were analyzed using a CHI650E electrochemical workstation. Thermogravimetric analysis (TGA) was conducted using a TG 309 Libra Classic thermogravimetric analyzer to monitor mass changes during calcination.

2.2.3 Catalytic Degradation Tests

3 mg of catalyst was dispersed into 50 mL of a TC solution (50 mg/L). The mixture was stirred in the dark for 30 min to ensure adsorption-desorption equilibrium between TC and the catalyst. Subsequently, 0.25 mL of a PS stock solution (100 mmol/L) was added to initiate the reaction. At predetermined time intervals, 0.5 mL of the reaction solution was sampled into centrifuge tubes, and 0.5 mL of methanol was immediately added to quench the reaction. The catalyst was removed using a 0.22 µm syringe filter, and the concentration of TC was determined via HPLC. The degradation performance was evaluated based on TC removal efficiency and the reaction rate constant. The TC degradation process was fitted using a pseudo-first-order kinetic model, as described in Equation (1):

$$\ln(C/C_0) = -k_{obs}t \qquad (1)$$

where kobs is the apparent rate constant (min^{-1}); tis the reaction time (min); Cis the pollutant concentration at time t; and C0 is the initial pollutant concentration. In catalyst stability tests, the catalyst was recovered by filtration using a PTFE membrane after the reaction, washed three times with deionized water, dried in an oven at 60 °C for 12 h, and reused in subsequent cycles.

In experiments investigating the effect of inorganic anions on the catalytic reaction, the concentration of each anion was fixed at 5 mmol/L. The initial pH of the solution was adjusted using 0.1 mol/L NaOH or H_2SO_4.

2.2.4 Reactive Species Trapping Experiments

In the trapping experiments, MeOH (500 mmol/L), TBA (500 mmol/L), FFA (1 mmol/L), and BQ (1 mmol/L) were added to the reaction system prior to the start of the catalytic reaction as quenchers for different reactive species.

3 Results and Discussion

3.1 Catalyst Structural Characterization

Based on previous tests, the as-prepared CDs carry a negative surface potential[21]. Upon addition of Cu^{2+}, electrostatic attraction caused the Cu^{2+} ions to adsorb onto the surface of CDs. Subsequently, urea was introduced, and a CDs composite precursor was synthesized via a hydrothermal method. As shown in the XRD pattern in Fig. 1(a), the diffraction peaks of this composite match well with those of $Cu_2(OH)_2CO_3$ (PDF#76-0660), indicating that the hydrothermal product is CDs/$Cu_2(OH)_2CO_3$. This precursor was calcined at 300 °C under N_2 atmosphere to yield the CDs/CuO$_x$-30 nanocatalyst. XRD analysis of the calcined samples revealed that the diffraction peaks of the sample prepared without CDs corresponded exactly to the characteristic peaks of CuO (PDF#80-0076). With the introduction of CDs, new diffraction peaks emerged in the calcined samples, signifying changes in phase composition. In the catalyst CDs/CuO$_x$-30, the diffraction peaks of CuO were significantly weakened, while new, strong peaks corresponding to Cu_2O appeared.

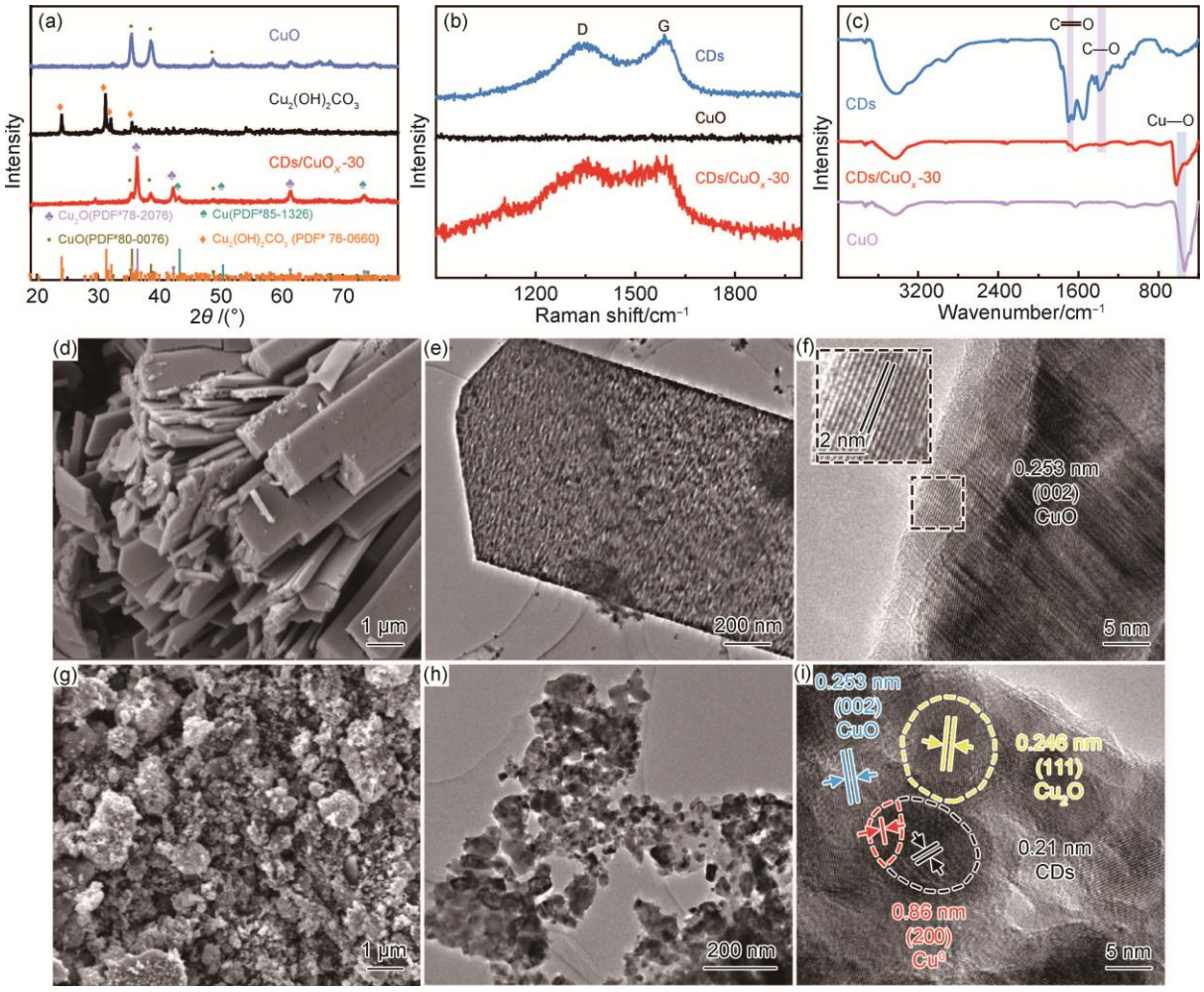

Figure 1 XRD patterns (a), Raman spectra (b), and FT-IR spectra (c) of different catalysts; SEM (d), TEM (e), and HRTEM (f) images of CuO; SEM (g), TEM (h), and HRTEM (i) images of CDs/CuO$_x$-30.

Additionally, diffraction peaks for Cu^0 were present, indicating that, driven by the reductive nature of CDs, partial CuO was reduced to Cu_2O and Cu^0 during the reaction. To verify the presence of CDs in CDs/CuO$_x$-30, Raman spectroscopy was performed on different catalysts. As seen in Fig. 1(b), two prominent peaks appear near 1377 cm^{-1} and 1592 cm^{-1}, attributed to the D band and G band of CDs, respectively[22]. The D band arises from structural defects in the material, while the G band corresponds to the stretching vibration of C–C bonds in carbon materials. This confirms the presence of carbonaceous material in CDs/CuO$_x$-30. FT-IR spectra of CDs, CuO, and CDs/CuO$_x$-30 are presented in Fig. 1(c).

The absorption bands near 3435 cm^{-1} and 1620 cm^{-1} are ascribed to the stretching and bending vibrations of surface-adsorbed water –OH groups. The band at 400 cm^{-1} corresponds to Cu–O vibrations[23]. Peaks observed in the spectra of CDs and CDs/CuO$_x$-30 within the ranges of 1600–1700 cm^{-1} and 1300–1400 cm^{-1} are assigned to the stretching vibrations of C=O and C–O, respectively[23]. These characteristic peaks are absent in the FT-IR spectrum of pure CuO, confirming the successful preparation of CDs/CuO$_x$-30. The morphology and structure of the prepared samples were characterized using SEM and TEM. Fig. 1(d) and 1(e) show that pure CuO consists of regularly shaped, micron-sized, lath-like aggregates. The high-resolution TEM (HRTEM) image reveals lattice fringes with a spacing of 0.253 nm, corresponding to the (002) plane of CuO (Fig. 1(f)). In contrast, Fig. 1(g) and 1(h) demonstrate that CDs/CuO$_x$-30 exhibits a significant morphological transformation, presenting as nanoscale, flocculent aggregates. This indicates that CDs influenced the nucleation and growth processes of the composite, resulting in reduced grain size. The HRTEM image in Fig. 1(i) clearly resolves lattice fringes with spacings of 0.186 nm, 0.253 nm, and 0.246 nm, corresponding to the (200) plane of Cu^0, the (002) plane of CuO, and the (111) plane of Cu_2O, respectively[22]. Furthermore, lattice fringes with a spacing of 0.21 nm, characteristic of CDs[24], are observed, indicating the successful incorporation of CDs into the sample.

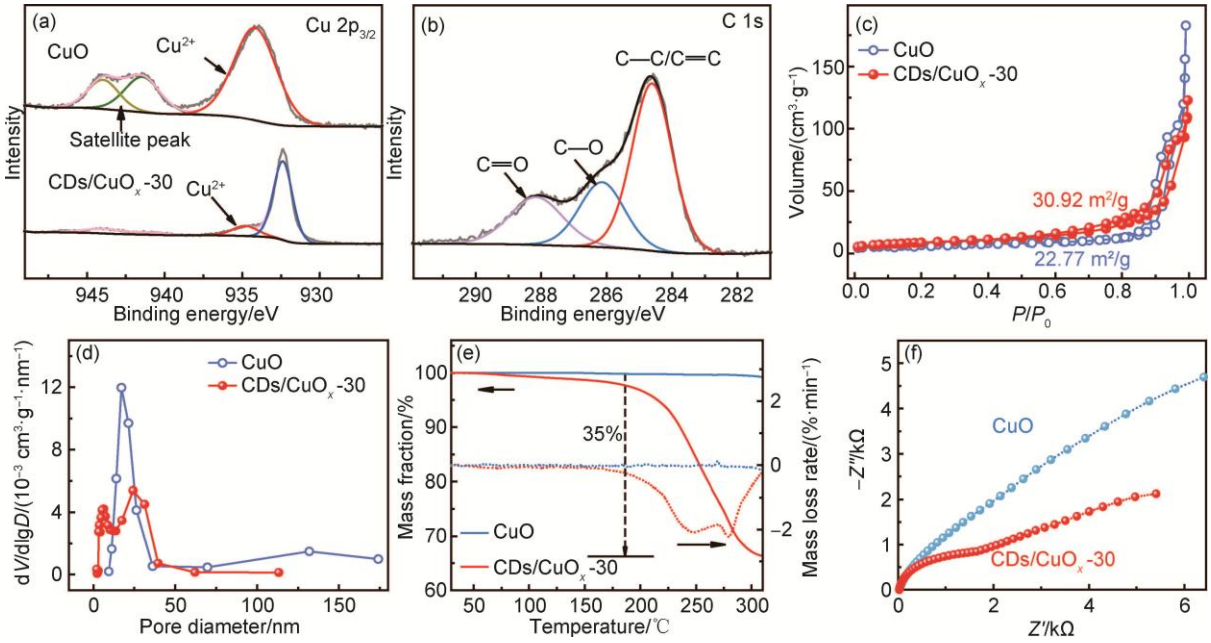

Figure 2 XPS Cu 2p spectra of CDs/CuO$_x$-30 and CuO (a); XPS C 1s spectrum of CDs/CuO$_x$-30 (b); N_2 adsorption-desorption isotherms (c) and corresponding pore size distribution plots (d); TGA thermograms (e); and electrochemical impedance plots (f) of CDs/CuO$_x$-30 and CuO.

XPS was employed to further investigate the elemental composition of CuO and CDs/CuO$_x$-30. Fig. 2(a) presents the Cu 2p high-resolution spectra. For pure CuO, only a peak at 934.4 eV corresponding to Cu^{2+} is observed, with no other discernible fitting peaks. In contrast, for CDs/CuO$_x$-30, the intensity of the Cu^{2+} peak at 934.7 eV is lower, and its associated satellite peaks are less pronounced. New fitting peaks emerge at 932.5 eV, attributable to Cu$^+$ and Cu^0[22]. This is due to the reductive nature of CDs, which facilitates the reduction of CuO to Cu_2O and Cu^0 during calcination under inert atmosphere. Fig. 2(b) shows the C 1s high-resolution spectrum of CDs/CuO$_x$-30. Peaks at binding energies of 284.4 eV, 286.2 eV, and 288.2 eV correspond to C–C, C–O, and C=O bonds,

respectively, which are characteristic of the carbon core structure and surface functional groups of CDs[23], further proving the presence of CDs. The specific surface area and pore size distribution of the two samples were determined via nitrogen adsorption-desorption measurements. As shown in Fig. 2(c), both isotherms are classified as type IV with H3-type hysteresis loops, indicative of typical mesoporous structures. The BET specific surface area of CDs/CuO$_x$-30 is 30.9 m^2/g, higher than that of CuO (22.7 m^2/g). As calculated from Fig. 2(d), the average pore volume of CDs/CuO$_x$-30 is 28 cm^3/g, far exceeding that of CuO (0.16 cm^3/g). The larger specific surface area and pore volume provide more potential adsorption sites for pollutants, facilitating the catalytic process. To elucidate the role of CDs, TGA was conducted to monitor potential physical and chemical changes in the precursors during pyrolysis. Fig. 2(e) shows that the mass loss of the CuO precursor during calcination at 300 °C under inert atmosphere is minimal. In contrast, the CDs/CuO$_x$-30 precursor exhibits a mass loss of approximately 35%, primarily attributed to deoxygenation reactions of the precursor and oxidation of CDs functional groups. Furthermore, EIS results indicate that the charge transfer resistance at the interface of CDs/CuO$_x$-30 is significantly lower than that of CuO (Fig. 2(f)). Consequently, electrons in the reaction system can more readily transfer to the catalyst surface to participate in chemical reactions.

3.2 Catalytic Performance Investigation

TC was employed as the target pollutant to evaluate the capability of the catalysts to activate PS for TC removal. As depicted in Fig. 3(a), neither CuO nor CDs alone could degrade TC within 60 min, even in the presence of 0.5 mmol/L PS. The CDs/$Cu_2(OH)_2CO_3$ composite formed during the hydrothermal process exhibited no PS activation ability. Under identical reaction conditions, the CuO+PS system achieved a TC removal rate of 42%, whereas the CDs/CuO$_x$-30+PS system increased the removal rate to 99%, representing a 2.4-fold improvement over CuO. The corresponding kobs values for different samples are shown in Fig. 3(b). The kobs of CDs/CuO$_x$-30 (0.066 min^{-1}) is 6.6 times that of CuO (0.010 min^{-1}).

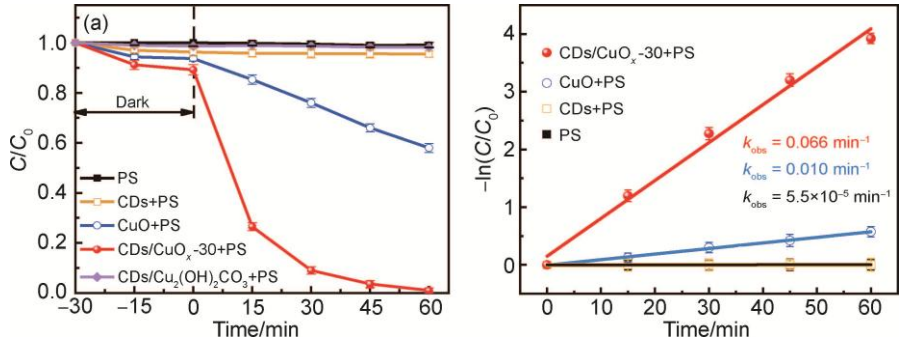

Figure 3 Efficiency of TC degradation by CuO and CDs/CuO$_x$-30 catalysts (a) and corresponding pseudo-first-order kinetic curves (b).

Table 1 compares the performance of CDs/CuO$_x$-30 with other reported catalysts for PS activation toward various pollutants. Since common pollutants vary widely—including phenol, norfloxacin (NOR), sulfamethoxazole (SMX), ofloxacin, p-chloroaniline (PCA), and progesterone (PGT)—and factors such as PS concentration and catalyst dosage significantly influence the apparent rate constant kobs, a modified kinetic parameter kM was calculated for fair comparison. As seen in Table 1[13,19,25-30], the km for the carbon-based catalyst three-dimensional graphene-like biochar (EGB-900) activating persulfate is merely 0.002 L/(min·g), while that for CuO is 0.0048 L/(min·g). Compositing carbon materials with copper-based catalysts, such as in Cu-CuO@C, elevates the km to 0.043 L/(min·g). Remarkably, the km value for the CDs/CuO$_x$ catalyst prepared in this work is 0.23 L/(min·g), demonstrating a superior activation rate.

Table 1. Comparison of CDs/CuO$_x$-30 with other catalysts in activating persulfate for pollutant degradation

Catalyst	Reaction Condition	Degradation Efficiency / %	km/ (L·min^{-1}·g^{-1})	Ref.
Cu-Cu_2O@C	[PS] = 4 mmol/L [Catalyst] = 0.5 g/L	100 (120 min)	0.043	[25]

	[Phenol] = 20 mg/L			
N-rGO/CuO	[PS] = 1 mmol/L [Catalyst] = 0.2 g/L [TC] = 20 mg/L	97 (90 min)	0.007	[26]
HEPs@CS	[PS] = 1.3 mmol/L [Catalyst] = 0.2 g/L [RhB] = 50 mg/L	99.7 (10 min)	0.22	[13]
Cu_3P/biochar	[PS] = 3 mmol/L [Catalyst] = 0.15 g/L [SMX] = 10 mg/L	100 (180 min)	0.002	[27]
CuFeBC	[PS] = 6 mmol/L [Catalyst] = 0.5 g/L [NOR] = 30 mg/L	94.5 (180 min)	0.0063	[19]
EGB-900	[PS] = 4 mmol/L [Catalyst] = 0.05 g/L [SMX] = 5 mg/L	95 (90 min)	0.002	[28]
CuO	[PS] = 2.5 mmol/L [Catalyst] = 0.5 g/L [PCA] = 0.5 mmol/L	100 (300 min)	0.0048	[29]
CuO/HNTs	[PS] = 7 mmol/L [Catalyst] = 0.5 g/L [PGT] = 2 mg/L	100 (480 min)	0.000011	[30]
CDs/CuO$_x$-30 (This work)	**[PS] = 0.5 mmol/L [Catalyst] = 0.06 g/L [TC] = 50 mg/L**	**99 (60 min)**	**0.23**	**This work**

Note: The modified kinetic parameter kmis calculated by dividing the apparent rate constant (kobs) by both the catalyst dosage and persulfate concentration, followed by multiplication with the pollutant concentration.

3.3 Analysis of Influencing Factors in the Reaction System

The effect of CDs content on PS activation performance was investigated by varying the amount of CDs added during synthesis. As shown in Fig. 4(a), under dark conditions, adsorption equilibrium was reached within 30 min. The adsorption capacity of TC by different catalysts showed no significant variation with changing CDs content. Upon PS addition, the degradation efficiency of CDs/CuO$_x$-20 was 92%, that of CDs/CuO$_x$-30 was 99%, and that of CDs/CuO$_x$-40 was 97%. Thus, CDs/CuO$_x$-30 exhibited the highest PS activation efficiency. Fig. 4(b) shows that the reaction rate constant kobs for the CDs/CuO$_x$-30 catalyst was 0.066 min^{-1}, 1.5 times that of CDs/CuO$_x$-20 (0.043 min^{-1}) and 1.2 times that of CDs/CuO$_x$-40 (0.051 min^{-1}). To understand the performance differences, the phase composition of catalysts with varying CDs loadings was analyzed via XRD. The XRD pattern in Fig. 4(c) reveals that CDs/CuO$_x$-20 comprises a two-phase structure of CuO and Cu_2O. As the CDs content increased, new diffraction peaks emerged at 43.31° and 50.44°, corresponding to Cu^0. CDs/CuO$_x$-30 exhibits a tri-phase structure consisting of CuO, Cu_2O, and Cu^0. CDs/CuO$_x$-40 is composed of Cu_2O and Cu^0, with the CuO peaks disappearing entirely. This indicates that increasing CDs content enhances the reductive effect on the catalyst composition. Consequently, CDs/CuO$_x$-30 was selected for subsequent experiments. The calcination atmosphere during synthesis also critically impacted the activation capability of CDs/CuO$_x$-30. As shown in Fig. 4(d), when calcined at 300 °C in air, the catalyst exhibited low PS activation ability, achieving only 60% TC removal. In contrast, calcination under N_2 atmosphere resulted in 99% TC removal. This difference likely relates to the phase composition formed under different atmospheres. Fig. 4(e) presents the XRD patterns of catalysts calcined under different atmospheres. Calcination in air yielded a single-phase product of CuO. Under N_2 protection, a multiphase structure comprising Cu_2O, CuO, and Cu^0 was obtained. During the reaction, Cu_2O can donate electrons to modulate the PS structure, exhibiting higher PS activation capability, whereas CuO interacts with PS much more weakly. The effect of calcination temperature was also investigated by varying the temperature under N_2 atmosphere. As shown in Fig. 4(f), at a calcination temperature of 250 °C, the catalyst exhibited the lowest TC removal rate (57%). Increasing the temperature to 300 °C maximized the removal rate

at 99%. Further increasing the temperature to 350 °C did not change the removal rate. Therefore, the optimal preparation parameters for CDs/CuO$_x$-30 were determined as a calcination temperature of 300 °C under N_2 atmosphere.

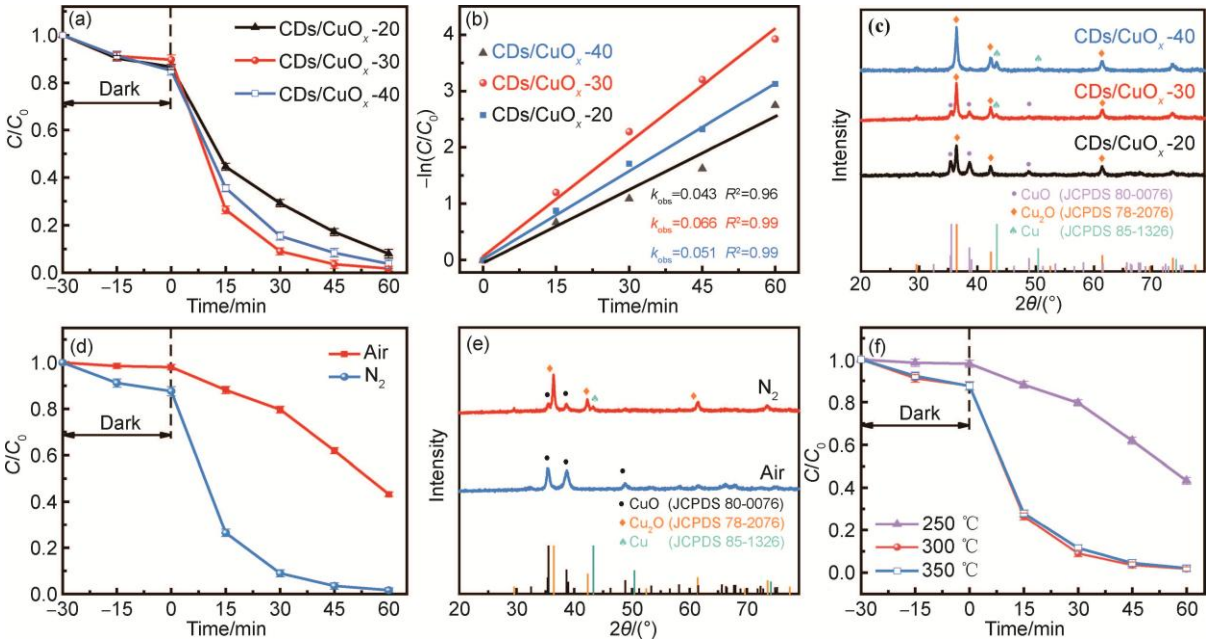

Figure 4 Comparison curves of TC removal efficiency (a) and pseudo-first-order kinetic curves (b) for catalysts with different CDs contents; XRD patterns (c) for catalysts with different CDs contents; comparison curves of TC removal efficiency (d) and corresponding XRD patterns (e) for catalysts calcined under different atmospheres; comparison curves of TC removal efficiency (f) for catalysts calcined at different temperatures.

The PS concentration in the reaction system significantly influences the catalytic reaction. Excess PS in the system can react with existing active species, leading to their consumption and reduced reaction efficiency. As shown in Fig. 5(a), with a constant catalyst concentration, increasing the PS concentration in the reaction solution from 0.1 mmol/L to 0.5 mmol/L enhanced the TC removal rate of CDs/CuO$_x$-30 from 30.4% to 98.2%. This is because a higher PS concentration provides more radicals for the degradation reaction. Further increasing the PS concentration to 1 mmol/L yielded no additional improvement in TC removal; thus, a PS concentration of 0.5 mmol/L was adopted for subsequent reactions. The initial pH of the solution affects the surface state of the catalyst and the ionization of organic pollutants; therefore, the catalyst's ability to activate PS is closely related to the initial pH. The effect of different pH values on TC removal by the CDs/CuO$_x$-30+PS system was investigated. As shown in Fig. 5(b), the optimal degradation performance was achieved without adjusting the initial solution pH (6.8). When the pH was adjusted to 3.0, the TC removal rate dropped to 70%; the rapid reaction rate observed in the first 15 min was attributed to massive leaching of copper ions. Under acidic conditions, both elemental copper and copper oxides are prone to metal ion leaching. When the solution pH was increased to 10, the TC removal rate decreased to 58%. On one hand, this may be due to changes in the surface charges of the catalyst, PS, and TC, leading to Coulombic repulsion between different phases that hindered contact and reduced catalytic efficiency. On the other hand, under alkaline conditions, $SO_4\cdot^-$ tends to transform into ·OH, which has a shorter lifetime, also disfavoring TC degradation. The influence of several inorganic anions on the CDs/CuO$_x$-30 activated PS degradation of TC was further studied. $SO_4\cdot^-$ and ·OH radicals readily react with halide ions. During PS activation, $SO_4\cdot^-$ and ·OH react with Cl^- to produce Cl· or $Cl_2\cdot^-$. Since the oxidation potentials of Cl· (2.09 V) and $Cl_2\cdot^-$ (1.36 V) are lower than that of $SO_4\cdot^-$ (2.5–3.1 V)[31], the addition of Cl^- typically reduces organic pollutant degradation efficiency. As shown in Fig. 5(c), adding Cl^- at a concentration of 5 mmol/L to the reaction solution did not diminish the activation capability of CDs/CuO$_x$-30. HCO_3^- can react with ·OH to generate $HCO_3\cdot$, but the reaction rate of $HCO_3\cdot$ with organic pollutants is low. Some reports suggest that HCO_3^- can chelate metal ions[31], reducing available active sites for the oxidant and thereby lowering catalytic activity. In this experiment,

adding HCO_3^- at the same concentration had no effect on TC degradation efficiency. Adding SO_4^{2-} at 5 mmol/L also had no impact on PS activation capability. However, the introduction of NO_3^- decreased the TC removal rate to 70%. NO_3^- does not react with PS and does not alter the solution pH. Generally, NO_3^- reacts with $SO_4^{\cdot-}$ and ·OH to form $NO_3^{\cdot}$ (2.3–2.5 V). Although the oxidation potential of $NO_3^{\cdot}$ is slightly lower than that of ·OH, it can still oxidize most organic pollutants[31].

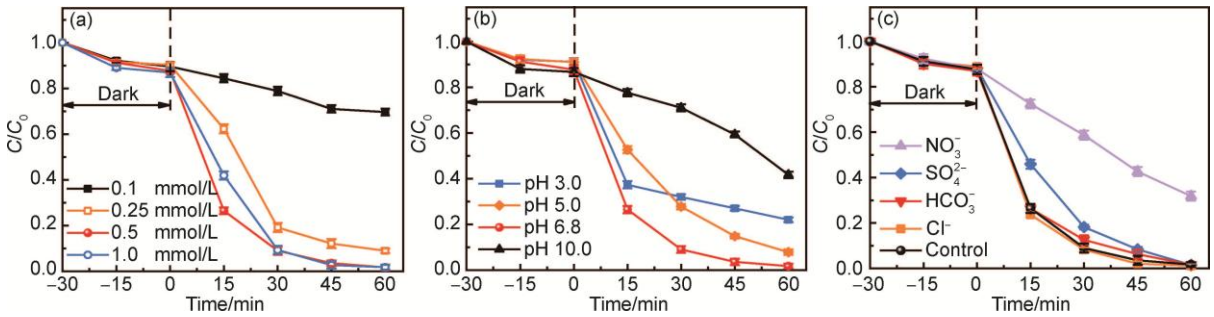

Figure 5 Effect of different PS concentrations (a), initial pH values (b), and inorganic anions (c) on TC degradation efficiency of CDs/CuO$_x$-30.

3.4 Catalyst Stability and Reusability

XRD patterns of CDs/CuO$_x$-30 before and after the catalytic reaction were collected, as shown in Fig. 6(a).

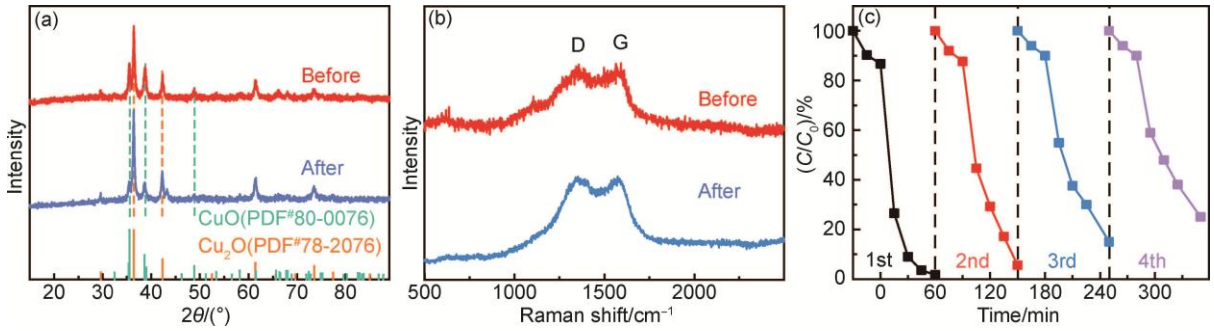

Figure 6 XRD patterns (a) and Raman spectra (b) of CDs/CuO$_x$-30 before and after catalysis; cycling stability of CDs/CuO$_x$-30 for TC degradation (c).

The diffraction peaks of CuO and Cu_2O persisted post-reaction, while the peak for Cu^0 disappeared. Fig. 6(b) presents the Raman spectra of CDs/CuO$_x$-30 before and after catalysis. The ID /IG ratio correlates with the proportion of defective or amorphous carbon structures relative to ordered graphitic or graphene structures in the sample. Post-reaction, the ID /IG ratio remained almost unchanged. The spent CDs/CuO$_x$-30 catalyst was recovered and subjected to consecutive cyclic tests. Fig. 6(c) shows that the PS activation efficiency of CDs/CuO$_x$-30 declined with increasing usage cycles. After four cycles, the TC removal rate decreased to 78%. This is likely related to the consumption of Cu species during the catalytic process. Nonetheless, the results demonstrate that CDs/CuO$_x$-30 possesses good reusability.

3.5 Analysis of Reactive Species

To identify the reactive species generated in the CDs/CuO$_x$-30+PS and CuO+PS systems, quenching experiments were conducted using MeOH, TBA, BQ, and FFA as quenchers[32-33] to determine the types of radicals and non-radicals involved. MeOH exhibits high reactivity toward both $SO_4^{\cdot-}$ and ·OH, while TBA is highly reactive only toward ·OH, with a reaction rate constant for $SO_4^{\cdot-}$ two orders of magnitude lower than that for MeOH. As shown in Fig. 7(a-1), in the CDs/CuO$_x$-30 activated PS system, upon addition of MeOH and TBA, the TC removal rate dropped from 99% to 33% and 38%, respectively. The apparent rate constants decreased from 0.066 min^{-1} to 0.004 min^{-1} and 0.006 min^{-1} (Fig. 7(a-2)). This infers the involvement of ·OH in the reaction, possibly alongside

a small amount of $SO_4^{\cdot -}$. The addition of BQ reduced the TC removal rate to 89%, indicating that the superoxide radical ($O_2^{\cdot -}$) also contributes to TC degradation. With the addition of FFA, the TC removal rate plummeted to 18.8%, demonstrating that singlet oxygen ($^1O_2$) plays a crucial inhibitory role in TC degradation (note: high FFA consumption indicates $^1O_2$ is a major contributor). Fig. 7(b-1) shows that in the CuO activated PS system, adding MeOH or TBA caused no significant change in TC removal rate, suggesting that $SO_4^{\cdot -}$, ·OH, and $O_2^{\cdot -}$ are not the primary active species in this system. However, adding FFA reduced the TC removal rate to 32%, and the apparent rate constant decreased from 0.018 min^{-1} to 0.013 min^{-1} (Fig. 7(b-2)), indicating that $^1O_2$ is the dominant reactive species in the CuO+PS system. Combined with the above results, the reactive species in the CDs/CuO$_x$-30+PS system include $^1O_2$, ·OH, and $O_2^{\cdot -}$, suggesting distinct degradation pathways exist between the CDs/CuO$_x$-30+PS and CuO+PS systems.

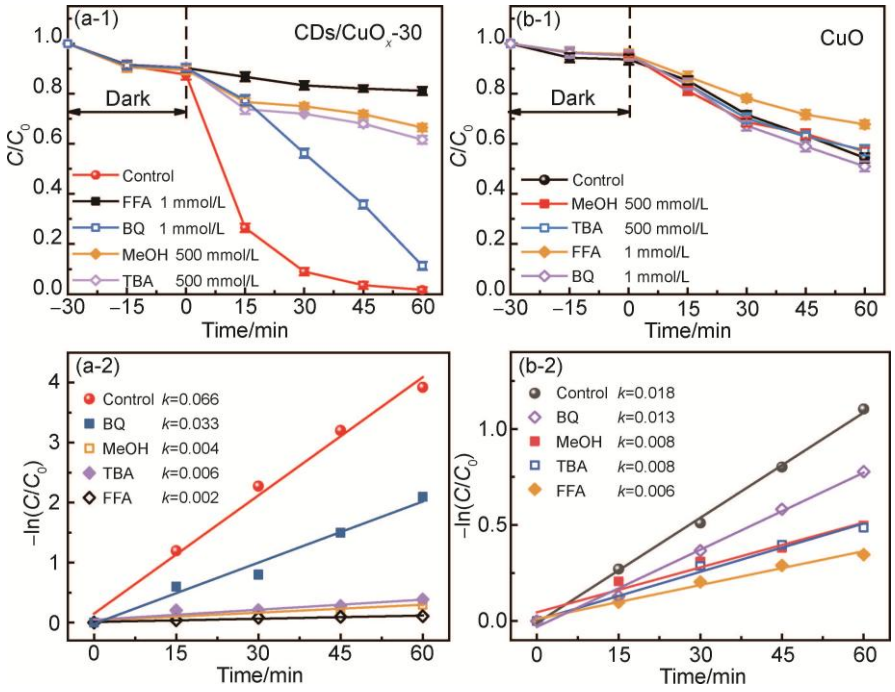

Figure 7 Effect of scavengers on TC degradation efficiency (1) and their pseudo-first-order kinetic curves (2) for CDs/CuO$_x$-30 (a) and CuO (b).

EPR spectroscopy was performed using DMPO and TEMP as spin traps to further verify the reactive species generated during the reactions in the CuO+PS and CDs/CuO$_x$-30+PS systems. The EPR results in Fig. 8(a) confirm that no DMPO-$SO_4^{\cdot -}$ or DMPO-·OH signals were detected in the CuO system; instead, a DMPO-X signal appeared, resulting from the rapid oxidation of DMPO-$SO_4^{\cdot -}$ and DMPO-·OH, presumably due to rapid PDS activation by Cu^{2+}. In the CDs/CuO$_x$-30+PS system, characteristic peaks of DMPO-·OH were detected, while the DMPO-$SO_4^{\cdot -}$ signal was weak, indicating the presence of ·OH and trace amounts of $SO_4^{\cdot -}$. $O_2^{\cdot -}$ also plays an important role in the degradation of many organic pollutants. Fig. 8(b) shows that DMPO-$O_2^{\cdot -}$ signals were observed in both the CDs/CuO$_x$-30+PS and CuO+PS systems, with the signal intensity in the CDs/CuO$_x$-30+PS system being 6.5 times higher than that in the CuO+PS system. Combined with the quenching experiment results, $O_2^{\cdot -}$ is not the primary active species responsible for TC degradation in the CDs/CuO$_x$-30+PS system. This is likely because $O_2^{\cdot -}$ exhibits weak reactivity toward most pollutants and does not directly degrade them. Fig. 8(c) shows that $^1O_2$ was present in both CDs/CuO$_x$-30+PS and CuO+PS systems. It is inferred that the main reactive species in the CDs/CuO$_x$-30+PS system are $^1O_2$ and ·OH.

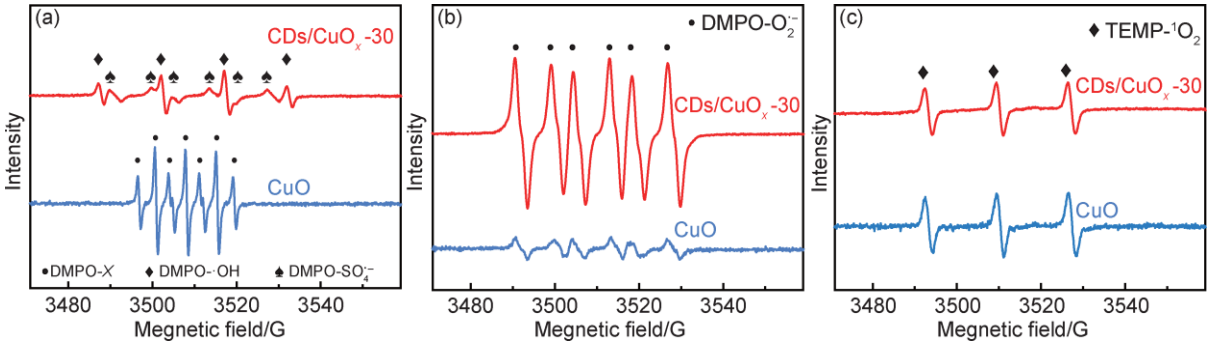

Figure 8 EPR spectra of DMPO-·OH, DMPO-$SO_4^{\cdot-}$, and DMPO-X (a); DMPO-$O_2^{\cdot-}$ (b); and TEMP-$^1O_2$ (c) for CuO and CDs/CuO$_x$-30 activated PS.

3.6 Discussion on Catalytic Mechanism

Previous literature reports that the primary active species for CuO activating PS to degrade organic pollutants is a non-radical surface-activated PS complex[34]. This surface-activated PS is a mild oxidant with an oxidation capacity lower than that of $SO_4^{\cdot-}$ or ·OH. This complex forms via outer-sphere interactions between persulfate and surface Cu^{2+} sites. According to the EPR results, the amount of $O_2^{\cdot-}$ radicals generated in the CuO system is low. It is inferred that the metastable CuO=PS complex reacts with H_2O to generate $^1O_2$[35], as described in Equation (2):

$$CuO{=}PS + H_2O \rightarrow CuO + 2SO_4^{2-} + {}^1O_2 + 4H^+ \quad (2)$$

To elucidate the role of Cu in PS activation, XPS was employed to analyze the chemical state of Cu species on the surface of CDs/CuO$_x$-30 after the reaction, aiming to identify potential active sites. As shown in Fig. 9(a), the relative proportion of Cu^{2+} increased from 15% to 18% post-reaction, indicating that Cu is indeed an active site.

$$Cu^0 + S_2O_8^{2-} \rightarrow Cu^+ + SO_4^{2-} + SO_4^{\cdot-} \quad (3)$$

$$Cu^0 + O_2 \rightarrow Cu^+ + O_2^{\cdot-} \quad (4)$$

$$2O_2^{\cdot-} + 2H^+ \rightarrow {}^1O_2 + H_2O_2 \quad (5)$$

$$Cu^+ + S_2O_8^{2-} \rightarrow Cu^{2+} + SO_4^{2-} + SO_4^{\cdot-} \quad (6)$$

$$O_2^{\cdot-} + Cu^{2+} \rightarrow O_2 + Cu^+ \quad (7)$$

$$O_2^{\cdot-} + S_2O_8^{2-} \rightarrow SO_4^{2-} + SO_4^{\cdot-} + O_2 \quad (8)$$

$$SO_4^{\cdot-} + H_2O \rightarrow {\cdot}OH + SO_4^{2-} + H^+ \quad (9)$$

It is inferred that Cu may react with PS according to Equation (3) to generate $SO_4^{\cdot-}$. Distinct from the CuO+PS system, the DMPO-$O_2^{\cdot-}$ signal intensity in the CDs/CuO$_x$-30+PS system was 6.5 times higher, suggesting the existence of a pathway for $O_2^{\cdot-}$ generation as per Equation (4). Combined with quenching experiments, $O_2^{\cdot-}$ is not the primary active species. Under acidic conditions, $O_2^{\cdot-}$ readily undergoes disproportionation to generate $^1O_2$, as per Equation (5). Cu_2O possesses strong electron-donating capability and can react with PS according to Equation (6) to generate $SO_4^{\cdot-}$. Since not all generated $O_2^{\cdot-}$ converts to $^1O_2$, and XPS analysis revealed only a minor change in the relative proportion of Cu^{2+} post-reaction, it is inferred that a reduction reaction of Cu^{2+} to Cu^+ occurs, as described in Equation (7). The Cu^+/Cu^{3+} reaction is unlikely here, as it generally occurs under neutral or alkaline conditions. Fig. 9(b) presents CV curves, confirming the presence of Cu^0/Cu^+ and Cu^+/Cu^{2+} redox transitions in the CDs/CuO$_x$-30 catalyst, whereas no distinct redox peaks were observed for pure CuO. Additionally, solution-phase $O_2^{\cdot-}$ may react with $S_2O_8^{2-}$ according to Equation (8) to generate $SO_4^{\cdot-}$. $SO_4^{\cdot-}$ subsequently reacts with H_2O according to Equation (9) to produce ·OH. Fig. 9(c) shows the amperometric i-tcurve, indicating that PS addition promotes current increase, signifying electron flow from the CDs/CuO$_x$-30

catalyst to PS. The addition of TC further elevates the current. Due to the multivalent states of Cu in CDs/CuO$_x$-30, electrons transfer from the catalyst to PS during reaction, triggering the generation of radical ·OH and non-radical $^1O_2$ to accomplish PS activation. The selective non-radical $^1O_2$ and the highly active radical ·OH act synergistically to degrade TC.

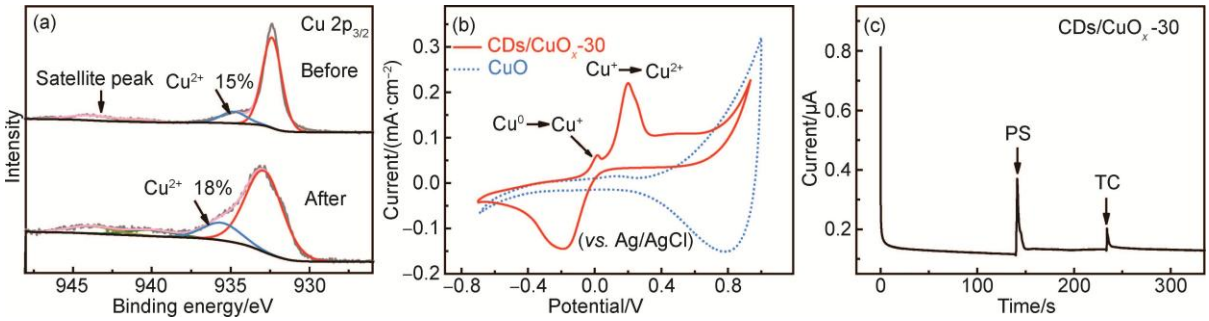

Figure 9 Cu 2p XPS spectra of CDs/CuO$_x$-30 before and after use (a); CV curves of CDs/CuO$_x$-30 and CuO (b); amperometric i-tcurve of CDs/CuO$_x$-30 in response to PS addition (c).

4 Conclusion

(1) A CDs/CuO$_x$ composite featuring a multiphase structure comprising Cu^0, Cu$_2$O, and CuO was successfully synthesized via a hydrothermal-calcination method, utilizing CDs to regulate the Cu valence state. This composite demonstrated excellent PS activation performance, achieving 99% TC degradation within 60 min—2.4 times higher than that of pure CuO—with an apparent rate constant kobs of 0.066 min^{-1}, which is 6.6 times that of CuO. (2) The high TC degradation efficiency of CDs/CuO$_x$ is attributed to Cu^0 acting as a continuous electron donor. This not only induces the generation of selective $^1O_2$ but, more crucially, promotes the Cu^{2+}/Cu$^+$ cycle, facilitating the production of more ·OH via PS activation. (3) After four consecutive catalytic cycles, the composite maintained a TC degradation rate of 78%, indicating good reusability. In the CDs/CuO$_x$+PS system, TC degradation is governed by the synergistic action of non-radical $^1O_2$ and radical ·OH (the primary species), with $O_2^{\cdot-}$ playing a secondary role.

References

[1] AHMAD F, ZHU D, SUN J. Environmental fate of tetracycline antibiotics: degradation pathway mechanisms, challenges, and perspectives[J]. Environmental Sciences Europe, 2021, 33(1): 64.

[2] ZHANG L, ZHANG Y, WEI J, et al. Perovskite LaFe$_x$Co$_{1-x}$O$_{3-\lambda}$ deposited SiO$_2$ catalytic membrane for deeply cleaning wastewater[J]. Chemical Engineering Journal, 2021, 403: 126386.

[3] ZHANG X, GUO W, NGO H H, et al. Performance evaluation of powdered activated carbon for removing 28 types of antibiotics from water[J]. Journal of Environmental Management, 2016, 172: 193-200.

[4] CHEN Z D, MENG G H, HAN Z H, et al. Interfacial anchoring cobalt species mediated advanced oxidation: degradation performance and mechanism of organic pollutants[J]. Journal of Colloid and Interface Science, 2022, 679: 67-78.

[5] YANG D, HONG P, HU Y, et al. Carbon framework-encapsulated copper oxide particles to activate peroxymonosulfate for the efficient degradation of tetracycline[J]. Applied Surface Science, 2021, 552: 149424.

[6] LIU Z, LAN H, WANG Y, et al. Highly efficient degradation of bisphenol A with persulfate activated by vacuum-ultraviolet/ultraviolet light (VUV/UV): experiments and theoretical calculations[J]. Chemical Engineering Journal, 2022, 429: 132485.

[7] LIU Y, WANG S, WU Y, et al. Degradation of Ibuprofen by thermally activated persulfate in soil systems[J]. Chemical Engineering Journal, 2019, 356: 799-810.

[8] ZHANG L, WANG T, ZHANG M, et al. Ultrasonically activated persulfate process for the degradation of phenanthrene in soil-washing effluent: experimental, DFT calculation and toxicity evaluation[J]. Journal of Environmental Chemical Engineering, 2024, 12(3): 113035.

[9] WANG J L, WANG S Z. Reactive species in advanced oxidation processes: formation, identification and rea ction mechanism[J]. Chemical Engineering Journal, 2020, 401: 126158.
[10] ZHU S, LI X, KANG J, et al. Persulfate activation on crystallographic manganese oxides: mechanism of singl et oxygen evolution for nonradical selective degradation of aqueous contaminants[J]. Environmental Scie nce & Technology, 2019, 53(1): 307-315.
[11] PAN Y, ZHANG Y, ZHOU M, et al. Enhanced removal of emerging contaminants using persulfate activated by UV and pre-magnetized Fe^o[J]. Chemical Engineering Journal, 2019, 361: 908-918.
[12] YANG J, YANG Y, GAO K, et al. Constructing S/N-vacancy- and Co/Mo-bimetallic-catalysts for tetracycline d egradation through peroxymonosulfate activation: evolution of active substance[J]. Environmental Resea rch, 2022, 282: 122051.
[13] CHEN Z, HUANG X, ZUO Y, et al. High-entropy perovskite embedded in carbon-based catalyst toward pero xymonosulfate activation to degrade Rhodamine B: Performance and mechanism insights[J]. Water Resea rch, 2022, 282: 123919.
[14] PAN J, WANG X, YANG X, et al. Insights into the enhanced oxidation of organic micropollutants by single-a tom Cu catalyst activated peroxydisulfate: valence-dominated nonradical pathway[J]. Applied Catalysis B: Environment and Energy, 2021, 351: 123997.
[15] XING S, LI W, LIU B, et al. Removal of ciprofloxacin by persulfate activation with CuO: a pH-dependent me chanism[J]. Chemical Engineering Journal, 2020, 382: 122837.
[16] HUANG M, HAN Y, XIANG W, et al. In situ-formed phenoxyl radical on the CuO surface triggers efficient pe rsulfate activation for phenol degradation[J]. Environmental Science & Technology, 2021, 55(22): 15361-1 5370.
[17] XU H, ZHANG Y, LIU X, et al. Non-radical activation of persulfate by CuO catalyst for degradation of antibio tics[J]. Journal of Environmental Chemical Engineering, 2022, 12(5): 113852.
[18] ZHANG Y, ZHANG C, ZHOU Z, et al. Degradation of ciprofloxacin by persulfate activation with CuO support ed on Mg-Al layered double hydroxide[J]. Journal of Environmental Chemical Engineering, 2021, 9(5): 106 178.
[19] CAI S, WANG T, WU C, et al. Efficient degradation of norfloxacin using a novel biochar-supported CuO/Fe_3O_4 combined with peroxydisulfate: insights into enhanced contribution of non-radical pathway[J]. Chemo sphere, 2021, 329: 138589.
[20] ZULFA L L, OKTAVIANTI N I, HIDAYAT A R P, et al. Recent advances of CDs-based ternary heterojunctions f or enhancing photocatalytic performance in the degradation of organic pollutants: a review[J]. Nano-Stru ctures & Nano-Objects, 2020, 37: 101104.
[21] DONG X, QI H, ZHAI Z, et al. Probing the fluorescence quenching mechanism of N-doped carbon quantum dots by inorganic ions[J]. Microchemical Journal, 2020, 197: 109854.
[22] ZHU Q, CHEN L, ZHU T, et al. Contribution of $^1O_2$ in the efficient degradation of organic pollutants with Cu^o /Cu_2O/CuO@N-C activated peroxymonosulfate: a case study with tetracycline[J]. Environmental Pollution, 2022, 342: 123064.
[23] PANG E, LI S, WU J, et al. Carbon-dot-induced oxygen vacancies in copper vanadate enabling persulfate ph otoactivation for tetracycline degradation[J]. Journal of Colloid and Interface Science, 2021, 683: 232-240.
[24] PANG E, LI S, WU J, et al. Carbon dots induce abundant oxygen vacancies in $CeVO_4$ for promoting photoca talytic selective hydrogenation of functionalized nitroarenes[J]. Inorganic Chemistry Frontiers, 2024, 11(7): 2128-2135.
[25] LI X, MIN X, HU X, et al. In-situ synthesis of highly dispersed Cu-CuO nanoparticles on porous carbon for th e enhanced persulfate activation for phenol degradation[J]. Separation and Purification Technology, 2021, 276: 119260.
[26] HE H, XIAO H, LIU C, et al. Efficient degradation of tetracycline with N-rGO/CuO catalysts under high salini ty condition via persulfate activation dominated by non-radical pathways[J]. Separation and Purification T echnology, 2020, 327: 124936.
[27] WANG X, LI W, WANG Y, et al. Efficient removal of sulfamethoxazole by biomass phosphorus-derived Cu_3 P/biochar catalyst combined with persulfate[J]. Separation and Purification Technology, 2021, 326: 12476 8.
[28] QI Y, GE B, ZHANG Y, et al. Three-dimensional porous graphene-like biochar derived from Enteromorpha a s a persulfate activator for sulfamethoxazole degradation: role of graphitic N and radicals transformation [J]. Journal of Hazardous Materials, 2020, 399: 123039.

[29] LIANG H Y, ZHANG Y Q, HUANG S B, et al. Oxidative degradation of p-chloroaniline by copper oxidate activated persulfate[J]. Chemical Engineering Journal, 2013, 218: 384-391.
[30] HUANG Z, LIN Q, LUO H, et al. Degradation of progesterone by coexisting free radical and nonradical pathways in the CuO/HNTs-PS system[J]. Chemical Engineering Journal, 2020, 398: 125458.
[31] WANG J, WANG S. Effect of inorganic anions on the performance of advanced oxidation processes for degradation of organic contaminants[J]. Chemical Engineering Journal, 2021, 411: 128392.
[32] ZHANG T, YANG Y, LI X, et al. Degradation of sulfamethazine by persulfate activated with nanosized zero-valent copper in combination with ultrasonic irradiation[J]. Separation and Purification Technology, 2020, 239: 116537.
[33] CHEN S, HUANG D, DU L, et al. Peroxymonosulfate activation by surface-modified bismuth vanadate for Ciprofloxacin abatement under visible light: insights into the generation of singlet oxygen[J]. Chemical Engineering Journal, 2022, 444: 136373.
[34] DING Y, FU L, PENG X, et al. Copper catalysts for radical and nonradical persulfate based advanced oxidation processes: certainties and uncertainties[J]. Chemical Engineering Journal, 2022, 427: 131776.
[35] WANG M M, CUI Y K, WEN J T, et al. Flexible regulation of persulfate activation mechanisms through tuning Cu valence in CuBTC-derived copper oxide catalysts for improved pollutant degradation[J]. Chemical Engineering Journal, 2022, 476: 146565.